

EVIDENCES OF CHROMOSPHERIC EVAPORATIONS IN THE DECEMBER 1, 2004 SOLAR FLARE

ZONGJUN NING¹, WENDA CAO², JING HUANG³, GUANGLI HUANG¹, YIHUA
YAN³, HENGQIANG FENG⁴

1 Purple Mountain Observatory, Nanjing 210008, China

*2 Center for Solar Terrestrial Research, New Jersey Institute of Technology, Newark, NJ
07102*

3 National Astronomy Observatory, Beijing 100012, China

*4 Department of Physics and Electron Science, Luoyang Normal University, Luoyang
471022, China*

ABSTRACT

In this paper, we present the radio and hard X-ray evidences of chromospheric evaporation during an M1.0 flare which occurred on December 1, 2004. The radio emission was observed by the Solar Broadband Radio Dynamic Spectrometer in China, which yielded dynamic spectra of decimetric emission. The hard X-ray emission was observed by *RHESSI*. In the radio spectra, the burst is characterized by two groups of the parallel-drifting structures, some of which change their drifting rates from positive to negative. Based on the standard flare model, we may explain these decimetric bursts in terms of chromospheric evaporation. On the other hand, *RHESSI* observations show that the hard X-ray emission in the energy range of 10-15 keV tend to rise from two footpoints to the looptop and eventually merge into a single looptop source, which is accepted as the evidence of the hard X-ray chromospheric evaporation. Such processes happened two time in this event. The drifting radio structures occurred between them, at the same time as the third hard X-ray peak observed at 25-50 keV.

Subject headings: Sun: flares — Sun: X-rays, gamma rays — Sun: radio radiation

1. INTRODUCTION

In the framework of the standard flare model, magnetic reconnection is regarded as the primary energy release mechanism to accelerate the particles in the current sheet located in

the corona. The accelerated particles (electrons) are then transported downward to the lower chromosphere along the field lines. From observations, the temporal fine structures in type IV radio bursts, especially, at the decimetric and microwave ranges, are generally regarded as the signature of radiation from these downward moving electrons or the waves driven by them. Hard X-ray emissions are thought to be the electron-ion bremsstrahlung produced by nonthermal electrons as they lose their energy in the lower corona or the chromosphere. Most of the nonthermal energy is transformed into thermal energy to heat the local plasma rapidly through Coulomb collisions. In the documents, the “Neupert effect” (e.g. Neupert 1968, Hudson 1991, Dennis & Zarro 1993, Dennis et al. 2003; Veronig et al. 2005; Ning 2008) is indicative of a strong link between the flare primary energy release and the coronal response. In the chromospheric layer, the resulting overpressure drives a mass flow upward along the loop at a speed of a few hundreds kilometers per second, the so-called “chromospheric evaporation”. The evaporation fills the flaring loop with a hot plasma up to a temperature of $\sim 10^7$ K, giving rise to the soft X-ray emissions. In other words, the chromospheric evaporation plays an important role to transport the thermal energy and the plasma from the chromospheric layers into the corona.

Observational evidences of chromospheric evaporation have been documented before at EUV, hard and soft X-ray and radio emissions, respectively. When the local chromospheric plasma is driven upward after heating, the fast upflows should be observed with blue-shift of EUV lines if a flare is near the disk center. Czaykowska et al. (2001) studied a two-ribbon flare in detail using SOHO/CDS observations. They found that the fast upflows are localized at the outsides of the flare ribbons. The similar results can also be found in other papers (Doschek et al. 1980; Feldman et al. 1980; Antonucci et al. 1982; 1984; Veronig et al. 2002; Li & Ding 2004; Berlicki et al. 2005; Milligan et al. 2006; Brosius & Holman 2007). Meanwhile, the hard X-ray sources risen from flare footpoints to looptop, recently observed by *RHESSI* (Lin et al. 2002), is thought to be the signature of the chromospheric evaporations. Liu et al. (2006) analyzed the spatial evolution of hard X-ray emission from an M1.7 flare on November 13, 2003. They found that the hard X-ray emission tends to rise above the footpoints and eventually merge into a single looptop source. From the observations, the typical timescale of hard X-ray source mergence motion is found to be about one minute (e.g. Liu et al. 2006; 2007). On the other hand, based on the plasma emission mechanism, the high temperature of the upflowing plasma considerably reduces the local free-free opacity, and a high-frequency cutoff is expected to be observed in the radio (decimetric) emissions due to the high-density regions behind the evaporation front. Aschwanden & Benz (1995) analyzed 21 flares and discovered the decimetric radio signatures for the chromospheric evaporation. They detected slowly drifting high-frequency cutoff at the frequency range between 1.1 and 3.0 GHz, with the drift rates of -41 ± 32 MHz s⁻¹, the

inferred speed is up to 360 km s^{-1} for the chromospheric evaporation. Numerical simulations for the observations of decimetric signatures of the chromospheric evaporation was carried out successfully by Karlicky (1998).

To gather the evidence for the chromospheric evaporations at the multi-wavelengths will be especially comprehensive to understand the physical processes. Up to now, however, this kind of works are rare. In this paper, we analyze the decimetric dynamic spectra of radio data, and spatial evolution of the hard X-rays for the December 1, 2004 flare. We detect the evidences of chromospheric evaporation for four times, two times at the radio, two times at the hard X-rays, respectively.

2. OBSERVATIONS AND MEASUREMENTS

The flare under study here is an M1.1 flare according to the *GOES* soft X-ray observations. It occurred on December 1, 2004 in AR 10708 (N06E20). This event was excellently observed by *RHESSI*. Figure 1 (bottom) shows the *RHESSI* and *GOES* light curves. The hard X-rays at the high energy band (25-50 keV) exhibit five peaks at 07:04:00, 07:05:40, 07:07:40, 07:10:20 and 07:13:40 UT, before the *GOES* soft X-ray reaching its maximum at 07:15:00 UT. *RHESSI* light curve at high-energy of 50-100 keV only shows the last three peaks. The steps in the *RHESSI* observations are due to the change of *RHESSI* attenuator state. For example, there are no attenuators in (A_0 state) before 07:07:40 UT, while the thin attenuator is in (A_1 state) after, except for two short periods near 07:24 and 07:36 UT, during which this attenuator briefly moves out. It is the night time of *RHESSI* after 07:37 UT.

2.1. The first evaporation at the hard X-rays

Figure 2 show the spatial evolution at the first and second hard X-ray peaks using the *RHESSI* CLEAN images at 10-15 keV. The front segments of detectors 3-8 excluding 7 are used for reconstructing the *RHESSI* images presented in this paper, yielding a spatial resolution of ~ 7 arcsec. This flare displays two footpoint sources at the hard X-rays, especially at 10-15 keV, while a looptop source at the soft X-rays of 6-10 keV at 07:04:20 UT. Figure 2 (left-top) shows the MDI magnetic field with the *RHESSI* X-ray contours at 6-10 keV and 10-15 keV. The south footpoint source (10-15 keV) is in the negative polarity field area, and the north source is near the positive field region, while the looptop source is located between them. Such morphology displays the typical characteristics of solar flare

in the X-ray observations. And it is consistent with the standard flare model, and with the previous findings with *YOHKOH* and *RHESSI* observations (e.g. Masuda et al. 1994; Sui et al. 2004). The looptop source is close to the north footpoint. Previous observations show that the looptop sources are often not symmetrically placed between footpoints (e.g. Liu et al. 2006). Then, both footpoint sources shift their positions at 07:04:20 UT, and move toward each other afterward. Finally, they merge into a single hard X-ray source at 07:05:20 UT. As shown in Figure 2, the mergence takes about 60 seconds, between 07:04:20–07:05:20 UT (marked by E_1 in Figure 1), which is corresponding to the interval between the first and second hard X-ray peaks (25-50 keV). However, the looptop source of 6-10 keV keeps the same position during this interval. In order to describe mergence motion of the hard X-ray sources, we measure the linear distance between the two footpoints at 10-15 keV. As given in Figure 2, the distance (L) is about 34.2 arcsec at 07:04:20 UT, then L is shortened to about 15.8 arcsec at 07:05:00 UT. At 07:05:20 UT, the two sources become one single source. The measured mergence speed is about 428 km s^{-1} . Note that we do not consider the projection effect here. This is the hard X-ray evidence of the first evaporation in this event. The previous observations show that the different energies of the X-rays could be of the different origin. The radiation of the energy 10-15 keV may be considered as thermal emission from the evaporated plasma or as nonthermal emission from the precipitating electrons, or, the most probable a mixture of both kinds of the radiation. Subsequently, the flare just shows a single source, as shown in Figure 2 (right-bottom), in the looptop with a broad energy band from 6-15 keV until the third peak of 07:07:40 UT. The flare displays two footpoint sources again at this time, as shown in Figure 5. Such morphology can be seen more clearly at 07:08:00 UT. The decimetric radio observations show the temporal structures on the dynamic spectra during this interval.

Concerning the spatial shifts of X-ray sources, it is necessary to perform more detailed study of the positions of X-ray sources and obtain more values of the velocities of plasma. If we assume that the evaporated plasma moves along a semi-circular loop, the obtained velocity of mergence at 07:04:20 – 07:05:20 UT (428 km s^{-1}) is the lower limit of the evaporation speed and, especially at the beginning, may not correspond to the evaporation speed. Therefore, we construct a model of a semi-circular flare loop connecting the hard X-ray footpoints and perpendicular to the solar surface and assuming the location of the flare on the disk, to try to estimate the evaporation speed (see e.g. Berlicki et al. 2002; Liu et al. 2006). The analyzed flare was observed close to the disk center. Three observed X-ray kernels, flare looptop source and two footpoint sources, are almost on the same line, which indicates the difficulty to construct three-dimension loop. Different from Liu et al. (2006) who constructed a semi-circular loop directly including the X-ray sources, we take two steps to get the brightness profiles along flare loop. Firstly, we use a rectangle to represent the

flare loop projection on the disk. This rectangle is choose large enough to try to include these kernels. We identify it here base on the 50% contour level of the 10-15 keV image. Its length is thought as the diameter of a semi-circular loop. We reconstruct the flare images with the PIXON algorithm (Metcalf et al. 1996; Hurford et al. 2002) at the energy band of 10-15 keV in a cadence of 4 seconds between 07:04:00 – 07:05:20 UT. After integration the brightness in the rectangle of each image, we obtain the evolution of 10-15 keV brightness profile along the loop diameter (projection distance). Figure 3 shows the results obtained from PIXON images with an integration time of 4 seconds from 07:04:00 UT to 07:05:00 UT for the energy band of 10-15 keV. Each profile is normalized by its maximum value, and the local maximum is marked by filled squares. The positions of two footpoint and looptop sources at 07:04:20 UT are plotted with dotted lines. As the CLEAN images showed in Figure 2, the looptop source is near the north footpoint, and the two footpoints (10-15 keV) are moving close, and finally merge into a single source which is close to the looptop source (6-10 keV). In order to measure the evaporation speed, we then have to know the evolution of brightness profile along the loop curve. Under an assumption of semi-circular loop, the loop curve length can approximately deduced from the circular diameter (or projection distance). For example, the curve distance at position of “i” along the loop is calculated from the projection at “i” as following, i.e. $L_{loop-curve}[i] \simeq R \times \arccos\left(\frac{R-L_{projection}[i]}{R}\right)$, where R is half of maximum projection distance ($2R = 75$ arcsec in Figure 3), and $i=0$ indicates the start, as the cross marked in Figure 2. ***Figure 3 shows the projection and loop curve distances as the first and second axis respectively. They have the same number of points, but with the different values. In this case, the points are unlinear and not uniformed along the loop curve axis. The tics are more spaced at the edges, and denser in the middle (around the loop-top). The numbers in the square bracket are corresponding to the projection positions of the first axis.*** Using the source positions with crosses in Figure 3, we estimate the north footpoint evaporation velocity from the maximum distance and maximum interval among these points, i.e., this source is located between $L_{projection}[42]$ and $L_{projection}[59]$, the corresponding loop curve distance is $L_{loop-curve}[59]-L_{loop-curve}[42] \sim 18.4$ arcsec. The maximum interval is about 4×11 seconds from Figure 3. Thus, we roughly obtain the evaporation velocity of 313 km s^{-1} . The dashed line is the linear fitting of these sources. Figure 4 plots *RHESSI* PIXON images for the different times corresponding to the eight profiles in Figure 3. As mentioned before, the rectangle is fixed on the images, and try to include the two footpoint sources and looptop source. It is possible that the X-ray kernels are outside this region, at least partly, as shown in Figure 4(d). We can obtain the different values of profiles if the rectangle width change narrow or wide, but the shape of normalized profiles in Figure 3 is independent of the rectangle width. Thus, the positions of filled squares are independent of the rectangle width as well.

2.2. Radio evidences of repeated chromospheric evaporations

The radio data that we use here is detected by Solar Broadband Radio Dynamic Spectrometer (*SBRS*) in China (Fu et al. 2004; Ji et al., 2005). For a detailed study of the fine structures in the decimetric and microwave bursts, a broad band radio spectrometer has been developed by the solar radio astronomical community of China in the past decade (Fu et al. 1995). It consists of 5 separate spectrometers covering the frequency range: 0.70-1.20 GHz, 1.100-1.340 GHz, 2.60-3.8 GHz, 4.50-7.50 GHz and 5.20-7.60 GHz, respectively. Same as *RHESSI*, these instruments also have an excellent coverage of the December 1, 2004 flare. This radio event is classified as type IV bursts with two series of parallel-drifting structures during the time interval between 07:07:10 - 07:08:15 UT (Huang et al. 2007). As the dynamic spectra shown in Figure 1 (top), a plenty of the fine structures are detected by 1.100-1.340 GHz spectrometer thanks to the high resolution mode of 4 MHz for the frequency channels and of 200 ms for the time resolution. There are two groups of parallel-drifting bands, i.e. D_1 (or D_2) and D_3 , before and after 07:07:40 UT, which is the same time of the third maximum of the X-ray flux at 25-50 keV. In other words, two groups of drifting radio structures happened on the rising and decay phases of the third hard X-ray peak. A detailed study of these fine structures can be found in the paper by Huang et al. (2007). In order to show these parallel-drifting structures clearly, Figure 1 (middle) shows the time derivative of the radio spectra. Thus, one drifting band can be divided into two strips, with the black and white color, respectively. The white strip is always followed by the black one. According to the dynamic spectra, these emission bands were drifting to the high frequencies at the beginning, then gradually turned towards the opposite direction. Meanwhile, some drifting bands disappeared. Such case can be well seen in the second group after 07:07:40 UT (the third hard X-ray peak time), in which there were eight parallel-drifting bands towards the high frequencies at the beginning, then only first two bands turned towards the low frequencies, the others show a persistent high-frequency cutoff. Such cutoff also drifts slowly to the low frequencies, parallel to the upward drifting bands.

We interpret such two groups of radio structures as the radio evidence of repeated chromospheric evaporations found before in solar flares (e.g. Aschwanden & Benz 1995). According to the standard model, magnetic reconnection can accelerate the electron beams downward along the magnetic loops from the corona to the chromosphere. The reverse-slope drifting bursts are possible the signatures of the radiation from these beams, which is similar as the interpretation of type III bursts reported before (e.g. Aschwanden et al. 1994; Aschwanden et al. 1995; Aschwanden & Benz 1995; Ning et al. 2000; Ning et al 2005). Meanwhile, the chromospheric evaporation front driven by the proceeding beams rises upward along the flare loops as well. The electron beams or their driven waves would stop their emissions due to the low temperature and high plasma density when they meet

the evaporation front. Observationally, the reverse-slope bursts would be cutoff at a certain frequency. Because the evaporation front rises upward continuously, such radio emission cutoff is expected to show a negative frequency-time drifting structure on the dynamic spectra (e.g. Aschwanden & Benz 1995). It is obvious that the observational frequency-time drift rate is related to the evaporation speed. In other words, from the radio observations, we can roughly estimate the evaporation speed. On the other hand, it is possible that the beams or their driven waves do not fade out, but propagate along with the evaporation front after changing their original direction. As shown in Figure 1, two parallel-drifting bands change their direction from positive to negative frequency-time drift rates in D3 group. The drifting rate of downward parallel-drifting bands is similar to each other, about 13 MHz s^{-1} . However, the upward parallel-drifting bands show different drifting rate, such as -4, -12 and -3 MHz s^{-1} for the bands marked by D_1 , D_2 and D_3 in Figure 1 (top). From these drifting rates, we infer the upward-directed velocities of chromospheric evaporation between $70\text{-}276 \text{ km s}^{-1}$ using the method used by Aschwanden & Benz (1995), when we assume the radio sources of these parallel-drifting structures have a speed of $0.001c$ (c is light speed). If we interpret the radio emission in terms of fundamental plasma emission, the observed frequency range corresponds to electron densities of $n_e = 1.5 - 1.8 \times 10^{11} \text{ cm}^{-3}$. These values are remarkably close to the typical values inferred from the radio data in the previous study (Aschwanden & Benz 1995).

Figure 5 plots the spatial evolution at 10-15 keV for the third and fourth X-ray peaks. It is worth to notice that the drifting structures visible in the radio spectra 07:07:20 - 07:08:10 UT are observed at the time (between 08:08:00 - 07:08:40 UT) when the south X-ray source is changing in *RHESSI* 10-15 keV images. In addition, as mentioned earlier, this happened at the time of the third maximum of X-ray flux (25 - 50 keV). It is particularly important that the south footpoint source was visible at 07:08:00 UT, and then seemed to disappear after 20 seconds. Such short timescale do not fit the evaporation scenario at the hard X-ray observations (e.g. Liu et al. 2006). So what could be the nature of the south footpoint at this time? Figure 6 (upper panels) plots the X-ray source contours at the three energies of 6-10 keV, 10-15 keV and 25-50 keV from 07:08:00 UT to 07:08:20 UT. From these *RHESSI* images, the north footpoint brightens at lower energy (6-15 keV), while the south one is brighter at a higher energy (10-50 keV). When the hard X-ray emissions were radiated at the higher energy, the south footpoint source appeared, especially at the time of 07:08:00 UT for the third hard X-ray peak.

2.3. The second evaporation in the hard X-rays

The decimetric drifting structures disappeared around 07:08:10 UT. Before the forth hard X-ray peak, i.e. at 07:09:00 UT, the flare displays two footpoint sources at 10-15 keV and a single looptop source at 6-10 keV as before. As shown in Figure 5, the looptop source is close, almost overlapped on the north footpoint source. After 07:09:00 UT, both footpoint sources are moving toward each other, especially, the south footpoint source is moving more clearly. About 100 seconds later, i.e., at 07:10:40 UT (marked by E_2 in Figure 1), both sources eventually merge into a single source at the same position as the looptop source of 6-10 keV. Same as before, we also measure the linear distance between the two footpoints at 10-15 keV. As given in Figure 5, the distance is $L \simeq 39.2$ arcsec at 07:09:00 UT, then it is shortened to ~ 25.0 arcsec at 07:10:20 UT (the forth hard X-ray peak time). Finally at 07:10:40 UT, two sources merge into one single source. We roughly measure the mergence speed to be about 294 km s^{-1} without considering the projection effect again. After 07:10:40 UT, this event displays a single source at the same position of looptop source. Meanwhile, the south footpoint source is moving towards the west, as the arrows shown in Figure 5.

We explain such mergence motion as the evidence of the second chromospheric evaporation shown in hard X-rays for this event. However, there is another possibility to interpret the spatial evolution in Figure 5. Especially, the south footpoint was not moving close to the north one, but just elapsed with the time. In such case, we can not explain the distance decrease between both footpoints as the evidence of the chromospheric evaporation. In order to rule out this possibility, Figure 6 also plots the MDI magnetic field with the *RHESSI* X-rays at three energy bands, i.e., 6-10 keV, 10-15 keV and 25-50 keV from 07:09:00 UT to 07:11:00 UT. At 07:09:00 UT, this flare displayed the standard flare picture again, with two footpoints (at 25-50 keV) located at the negative and near positive polarity field regions, respectively, a looptop source (at 6-10 keV) between them. The 10-15 keV X-rays show two sources, which are close to the two footpoints, and seem to be located at the chromosphere layers between the heights corresponding to the X-ray emissions at 6-10 keV and 25-50 keV. In the following time, the south footpoint at 10-15 keV was moving close to the north one, while the south footpoint at 25-50 keV kept to stay at the same position as before, the north footpoint disappeared. This fact proves that the south footpoint source of this flare keeps to stay at the same position, i.e. at 25-50 keV, while the 10-15 keV source does be moving close during the interval from 07:09:00 UT to 07:10:40 UT. Therefore, both footpoints of the flare observed at 10-15 keV rise and the distance between them is decreased, and eventually merges into a single looptop source, which is the evidence of the second chromospheric evaporation process in hard X-ray observations. Also, the flare rises its sources at 10-15 keV along the flare loops, especially, the south footpoint source, the projection effect probably results into its position shifting toward west on the solar disk.

Using the same method noted earlier in Figure 3, **Figure 7 plots the evolution of the 10-15 keV brightness profiles along the projection (first axis) and loop curve (second axis) distances obtained from PIXON images at 10-15 keV with an integration time of 4 second from 07:08:40 UT to 07:10:40 UT. Note $2R=70$ arcsec here.** The white rectangle in Figure 5 represents the loop projection. The north (or south) footpoint evaporation velocity is estimated from the maximum distance (from the second axis) and the maximum interval among the black squares marked by plus (or cross). The points marked by star are used for both sources. The maximum distance among these points is $L_{loop-curve}[44]-L_{loop-curve}[32] \sim 12.1$ arcsec for the north footpoint source, while $L_{loop-curve}[39]-L_{loop-curve}[16] \sim 24.1$ arcsec for the south one. The maximum interval is about 4×13 seconds for both sources. As shown in Figure 7, we approximately obtain the velocity of 175 km s^{-1} for the north footpoint source and 347 km s^{-1} for the south one. Same as the first evaporation process shown in Figure 3, the evaporation speed is asymmetric along the flare loop. This could be caused that the X-ray looptop source is not really on the loop top, but close to the north footpoint.

3. CONCLUSIONS AND DISCUSSIONS

We present the radio and hard X-ray observations of the December 1, 2004 flare, which shows the evidences of chromospheric evaporation at both decimetric and hard X-ray emissions. From the *RHESSI* imaging, this flare risen its both footpoints and eventually merge into a single looptop source at 10-15 keV. This process occurred two times, i.e. between 07:04:20 - 07:05:20 UT and 07:09:00 - 07:10:40 UT, which suggests that there are two independent chromospheric evaporations. If we compare the spatial positions of footpoint sources for these twice processes, as shown in Figures 2 and 5, the flare shifts their footpoint position from the first to the second evaporation, especially, about 20 arcsec from east to west for the south footpoint source. However, the looptop source at 6-10 keV almost keeps the same position during the flare. This indicates that there is a spatial separation of these twice chromospheric evaporation processes observed in hard X-rays. Consistent with the previous findings (e.g. Liu et al. 2006), the timescale of evaporation process is about 60-100 seconds in hard X-rays of 10-15 keV. After constructing a semi-circular flare loop, we roughly estimate the evaporation speeds from 175 to 347 km s^{-1} , which is typical value for the chromospheric evaporation in the hard X-ray observations. In this event, the evaporation velocities are different for two footpoint sources, which could be related to the fact that the electron precipitating site (looptop source) is not really on the loop top.

It is interesting that the decimetric radio dynamic spectra show the evidences of other

twice chromospheric evaporation between them. The radio bursts show parallel-drifting structures with the positive frequency-time drift rate. Due to the low-temperature and high-density in the chromospheric evaporation front, either these radio structures change their drifting directions from the positive to negative frequency-time drifting, or stop their emissions to show a high-frequency cutoff with a negative drifting. From these frequency-time drift rate, we roughly estimate that the evaporation speed is about 70-276 km s⁻¹. However, Huang et al. (2007) tried to explain the observational characteristics of the radio event with zebra pattern theory (e.g. Kuijpers 1975; Zhelezniakov & Zlotnik 1975; Isliker & Benz 1994; Chernov et al. 2005). We think that this decimetric observation shows some features being consistent with the radio signatures of chromospheric evaporation in the examples by Aschwanden & Benz (1995). Our interpretation of this radio event in terms of chromospheric evaporation can explain several observational properties: (1) the slow negative drifting of the high-frequency cutoff, (2) the change of the parallel-drifting bands from positive to negative, (3) the slow negative drifting of the parallel-drifting bands. The two groups of parallel-drifting structures, such as D1 (or D2) before 07:07:40 UT, and D3 after 07:07:40 UT, indicates the time separation of twice chromospheric evaporation processes. These parallel-drifting band maybe represent a certain wave pattern. It is possible that these waves co-move with the density or temperature structure of the chromospheric evaporation when they meet the front. The changing of drifting rates from positive to negative is the radio signature of this process. It is possible that the drifting radio structures are correlated with the third hard X-ray maximum at 25-50 keV. As mentioned before, they are occurred at the same time. However, the hard X-ray observations seem not to fit the evaporation scenario, while the radio structures do.

Thus, the December 1, 2004 flare shows the evidences of the chromospheric evaporation four times at the radio and hard X-ray observations. It is possible such multiple evaporation processes are independent to each other. As shown in Figure 1, these four processes continuously occur with the time, and may correspond to the first, third and forth hard X-ray peaks. Whatever, it is first time to observe the multiple chromospheric evaporation in a solar flare. More examples of the multi-wavelengths observations of multiple chromospheric evaporation are necessary to continue this work.

We thank the anonymous referee for the valuable comments to improve this manuscript. W. Cao gratefully acknowledges the support of NSF through ATM-0847126, ATM-0745744, and NASA through NASA-NNX08BA22G. This work is also supported by NSF of China under grants 10603014, 10843005, 10833007, 40804034, 973 Program under grant 2006CB806302, and CAS Project under grant KJCX2-YW-T04.

REFERENCES

- Antonucci, E., et al. 1982, *Sol. Phys.*, 78, 107
- Antonucci, E., Gabriel, A. H., & Dennis, B. R. 1984, *ApJ*, 287, 917
- Aschwanden, M. J., Benz, A. O., & Montello, M. L. 1994, *ApJ*, 431, 432
- Aschwanden, M. J., & Benz, A. O. 1995, *ApJ*, 438, 997
- Aschwanden, M. J., Benz, A. O., Dennis, B. R., & Schwartz, R. A. 1995, *ApJ*, 455, 347
- Berlicki, A., Rudawy, P., Siarkowski, M., & Jurecki, M. 2002, *Advances in Space Research*, 30, 605
- Berlicki, A., Heinzl, P., Schmieder, B., Mein, P., & Mein, N. 2005, *A&A*, 430, 679
- Brosius, J. W., & Holman, G. D. 2007, *ApJ*, 659, L73
- Chernov, G. P., Yan, Y. H., Fu, Q. J., & Tan, C. M. 2005, *A&A*, 437, 1047
- Czaykowska, A., Alexander, D., & De Pontieu, B. 2001, *ApJ*, 552, 849
- Dennis, B. R., & Zarro, D. M. 1993, *Sol. Phys.*, 146, 177
- Dennis, B. R., Veronig, A., Schwartz, R. A., Sui, L., Tolbert, A. K., Zarro, D. M., & Rhesi Team 2003, *Advances in Space Research*, 32, 2459
- Doschek, G. A., Feldman, U., Kreplin, R. W., & Cohen, L. 1980, *ApJ*, 239, 725
- Dulk, G.A. and Marsh, K.A.: 1982, *Astrophys. J.* **259**, 350.
- Feldman, U., Doschek, G. A., Kreplin, R. W., & Mariska, J. T. 1980, *ApJ*, 241, 1175
- Fu, Q., Qin, Z., Ji, H., & Pei, L. 1995, *Sol. Phys.*, 160, 97
- Fu, Q., et al. 2004, *Sol. Phys.*, 222, 167
- Huang, J., Yan, Y., & Liu, Y. 2007, *Advances in Space Research*, 39, 1439
- Hudson, H. S. 1991, *BAAS*, 23, 1064
- Hurford, G. J., et al. 2002, *Sol. Phys.*, 210, 61
- Isliker, H., & Benz, A. O. 1994, *A&AS*, 104, 145
- Ji, H.-R., et al. 2005, *Chinese Journal of Astronomy and Astrophysics*, 5, 433

- Karlicky, M. 1998, *A&A*, 338, 1084
- Kuijpers, J. 1975, *Sol. Phys.*, 44, 173
- Lin, R. P., et al. 2002, *Sol. Phys.*, 210, 3
- Li, J. P., & Ding, M. D. 2004, *ApJ*, 606, 583
- Liu, W., Liu, S., Jiang, Y. W., & Petrosian, V. 2006, *ApJ*, 649, 1124
- Liu, W., Petrosian, V., Dennis, B. R., & Jiang, Y. W. 2007, *ArXiv e-prints*, 709, arXiv:0709.1963
- Masuda, S., Kosugi, T., Hara, H., Tsuneta, S., & Ogawara, Y. 1994, *Nature*, 371, 495
- Metcalf, T. R., Hudson, H. S., Kosugi, T., Puetter, R. C., & Pina, R. K. 1996, *ApJ*, 466, 585
- Milligan, R. O., Gallagher, P. T., Mathioudakis, M., & Keenan, F. P. 2006, *ApJ*, 642, L169
- Neupert, W. M. 1968, *ApJ*, 153, L59
- Ning, Z., Fu, Q., & Lu, Q. 2000, *Sol. Phys.*, 194, 137
- Ning, Z., Ding, M. D., Wu, H. A., Xu, F. Y., & Meng, X. 2005, *A&A*, 437, 691
- Ning, Z. 2008, *Sol. Phys.*, 248, 99
- Sui, L., Holman, G. D., & Dennis, B. R. 2004, *ApJ*, 612, 546
- Veronig, A., Vršnak, B., Dennis, B. R., Temmer, M., Hanslmeier, A., & Magdalenic, J. 2002, *A&A*, 392, 699
- Veronig, A. M., Brown, J. C., Dennis, B. R., Schwartz, R. A., Sui, L., & Tolbert, A. K. 2005, *ApJ*, 621, 482
- Zheleznyakov, V. V., & Zlotnik, E. Y. 1975, *Sol. Phys.*, 44, 461

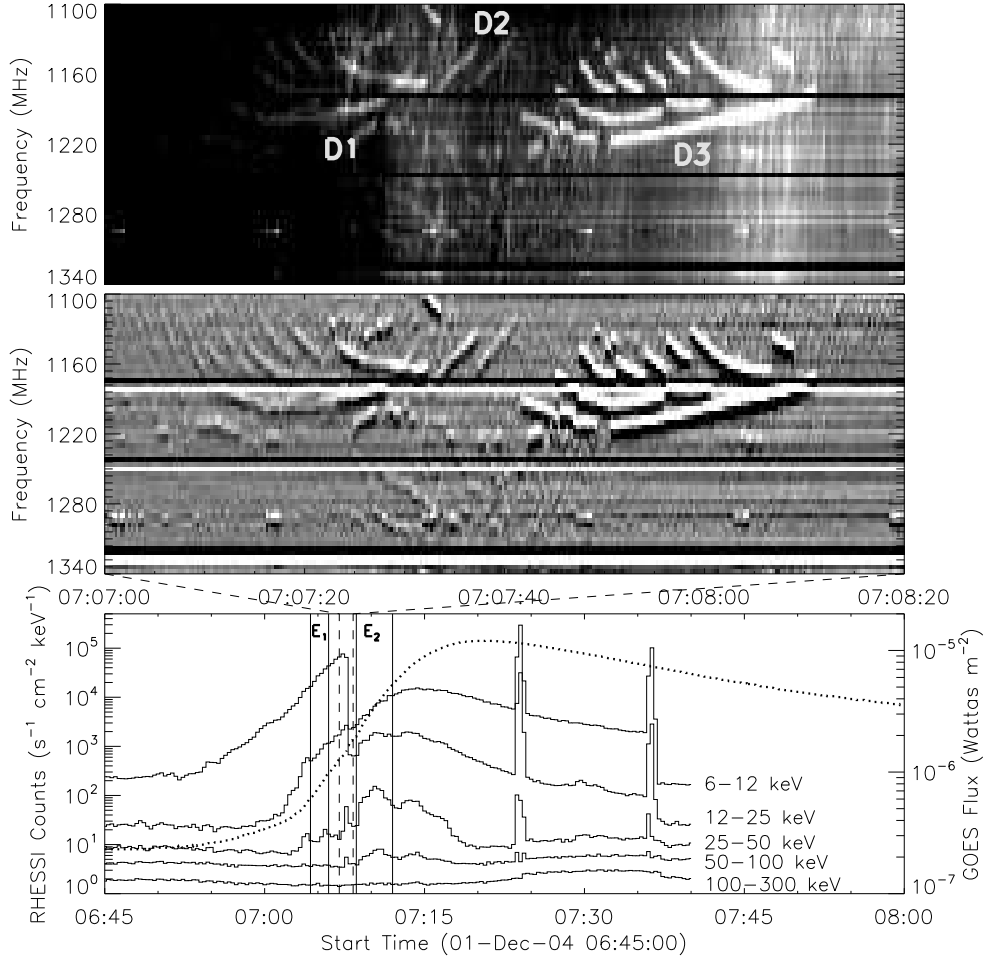


Fig. 1.— Radio dynamic spectra (*top*) and their time derivative (*middle*) of SBRS radio data for the December 1, 2004 solar flare, which is plotted in the frequency range of 1.100-1.340 GHz, with a time resolution of 200 ms. Two groups of parallel-drifting structures are marked by D₁ (or D₂) and D₃. The bottom frame shows the *GOES* soft X-ray flux at 1-8 Å (dotted line) and *RHESSI* light curves in five energy bands 6-12, 12-25, 25-50, 50-100 and 100-300 keV, with corresponding scaling factors 1, 1, 2, 5 and 5, respectively. The time binning is 20 s. Spatial evolutions at two time intervals marked E₁ (07:04:20 - 07:05:20 UT) and E₂ (07:09:00 - 07:10:40 UT) are shown in Fig. 2 and 4 respectively.

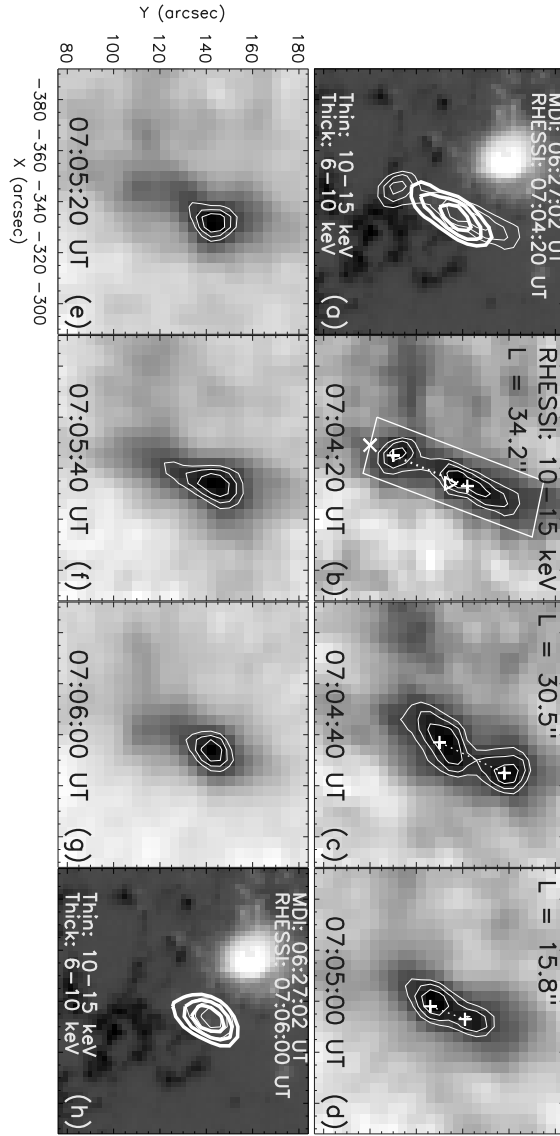


Fig. 2.— MDI map of magnetic field at 06:27:02 UT, showing the sunspots with positive (*white*) and negative (*black*) polarities with *RHESSI* X-ray contours at 07:04:20 UT (a), or at 07:06:00 UT (h). *RHESSI* CLEAN images (b, c, d, e, f, g) at six different times (the interval of E_1 in Fig. 1) for the December 1, 2004 flare. Energy binning band is 10-15 keV. All contour levels are set at 70%, 80%, and 90% of the maximum brightness for 10-15 keV (*thin lines*) or 6-10 keV (*thick lines*) images. In panel (b), the white rectangle is considered as the loop projection on the disk, and the cross indicates the start point of the distance in Fig.3. The pluses represent the positions of maximum bright at both footpoints, and the values of L measure the distance (*dashed lines*) between them. The front segments of detectors 3-8 excluding 7 are used for reconstructing these images.

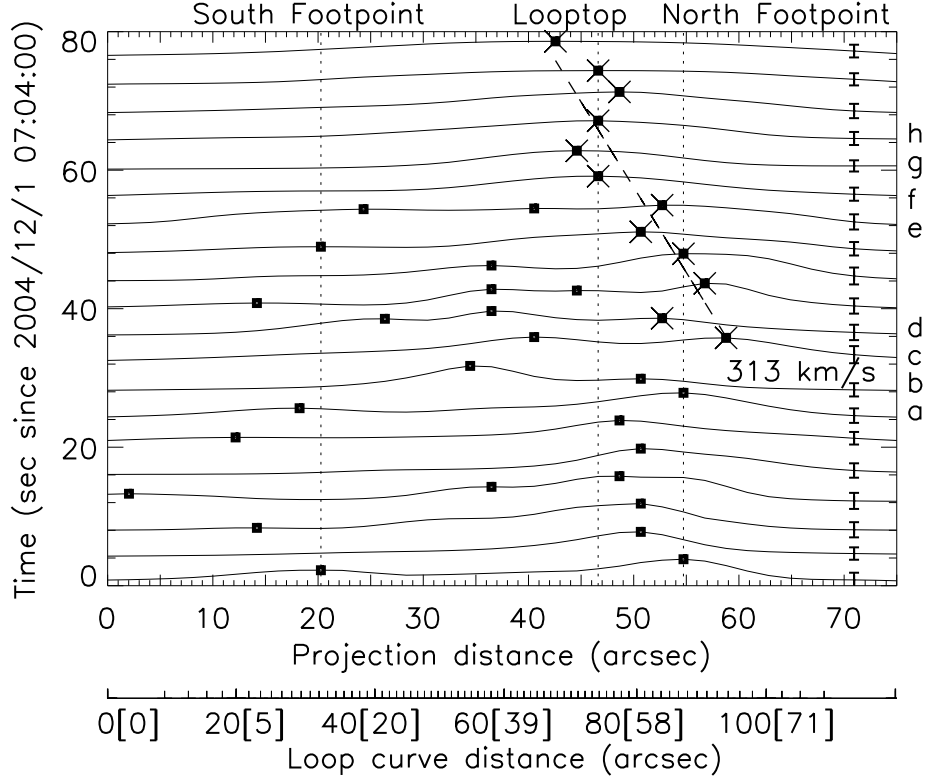


Fig. 3.— *Evolution of the 10-15 keV brightness profile along the projection distance (first axis) and the loop curve distance (second axis) in a cadence of 4 s, starting at 07:04:00 UT. The numbers in the square bracket along the second axis are corresponding to the projection positions on the first axis. Each profile is an integration of the white box region in Fig. 2, and it is normalized to its own maximum. The black squares mark the local maximum, and the three vertical lines mark the corresponding positions of X-ray sources in Fig. 2. The error bar on each curve indicates an estimated standard deviation of the profile. The north footpoint evaporation velocity of 313 km s^{-1} is estimated from maximum distance (from the second axis) and maximum interval among the points marked with cross. Dashed line is the linear fitting of them (see details in text).*

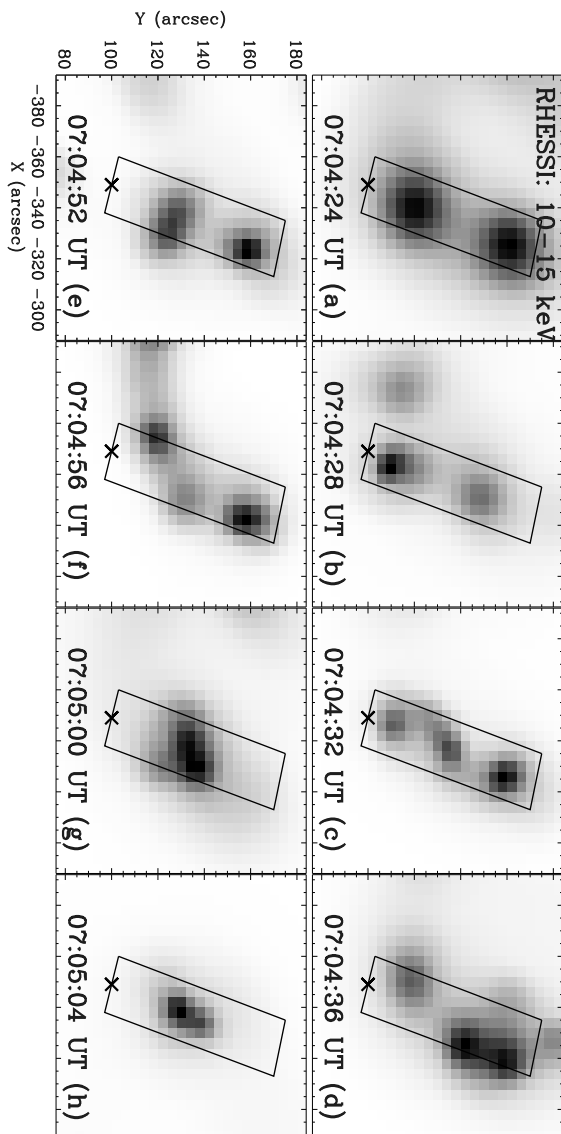


Fig. 4.— *RHESSI* PIXON images for different times. The rectangles and pluses are same as in Fig.2(b). The profiles of their integrated intensities are marked by a, b, c, d, e, f, g, h in Fig. 3. The front segments of detectors 3-8 excluding 7 are used for reconstructing these images.

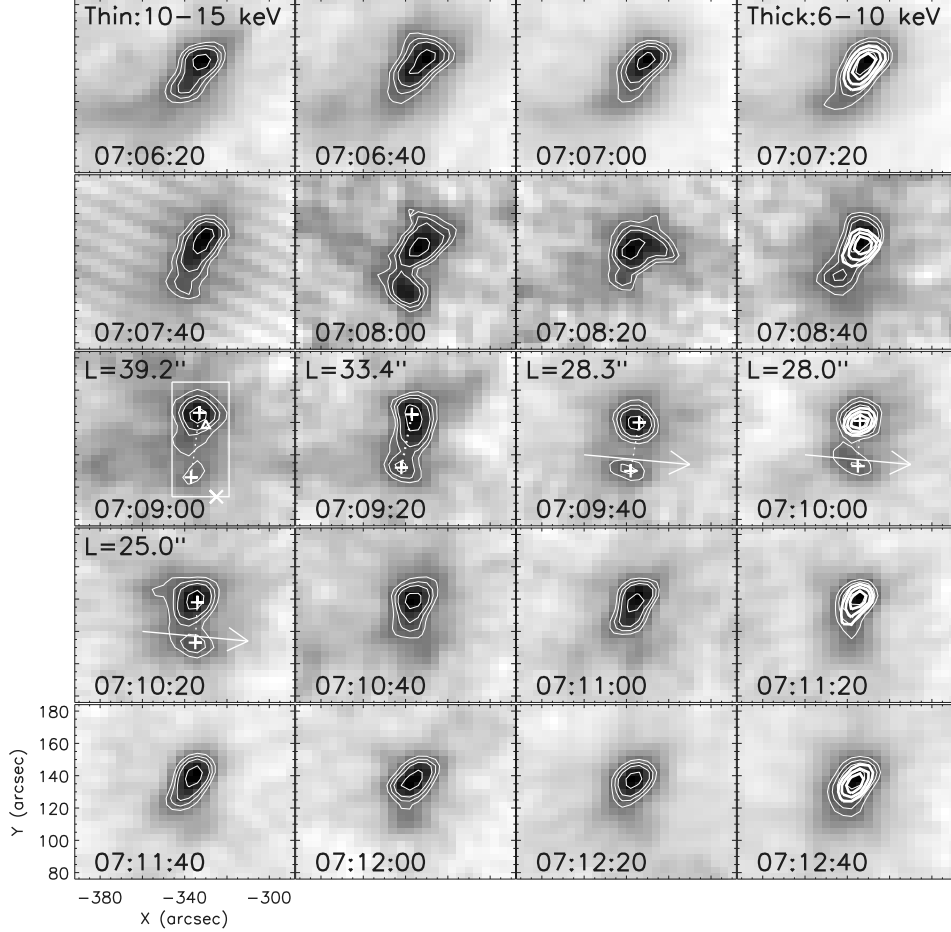


Fig. 5.— As in Fig. 2, but only *RHESSI* images for the time interval of E_2 in Fig. 1 and at energy band of 10-15 keV. When both footpoints are moving close together (as shown with dashed lines), the south footpoint source shifts its positions from east to west as arrows. The white rectangle is constructed as the loop projection on the disk again, and the cross indicates the start point of the distance in Fig.6. The contour levels are set at 50%, 60%, 70%, and 90% of the maximum brightness at 10-15 keV (*thin lines*), and at 70%, 80%, and 90% at 6-10 keV (*thick lines*).

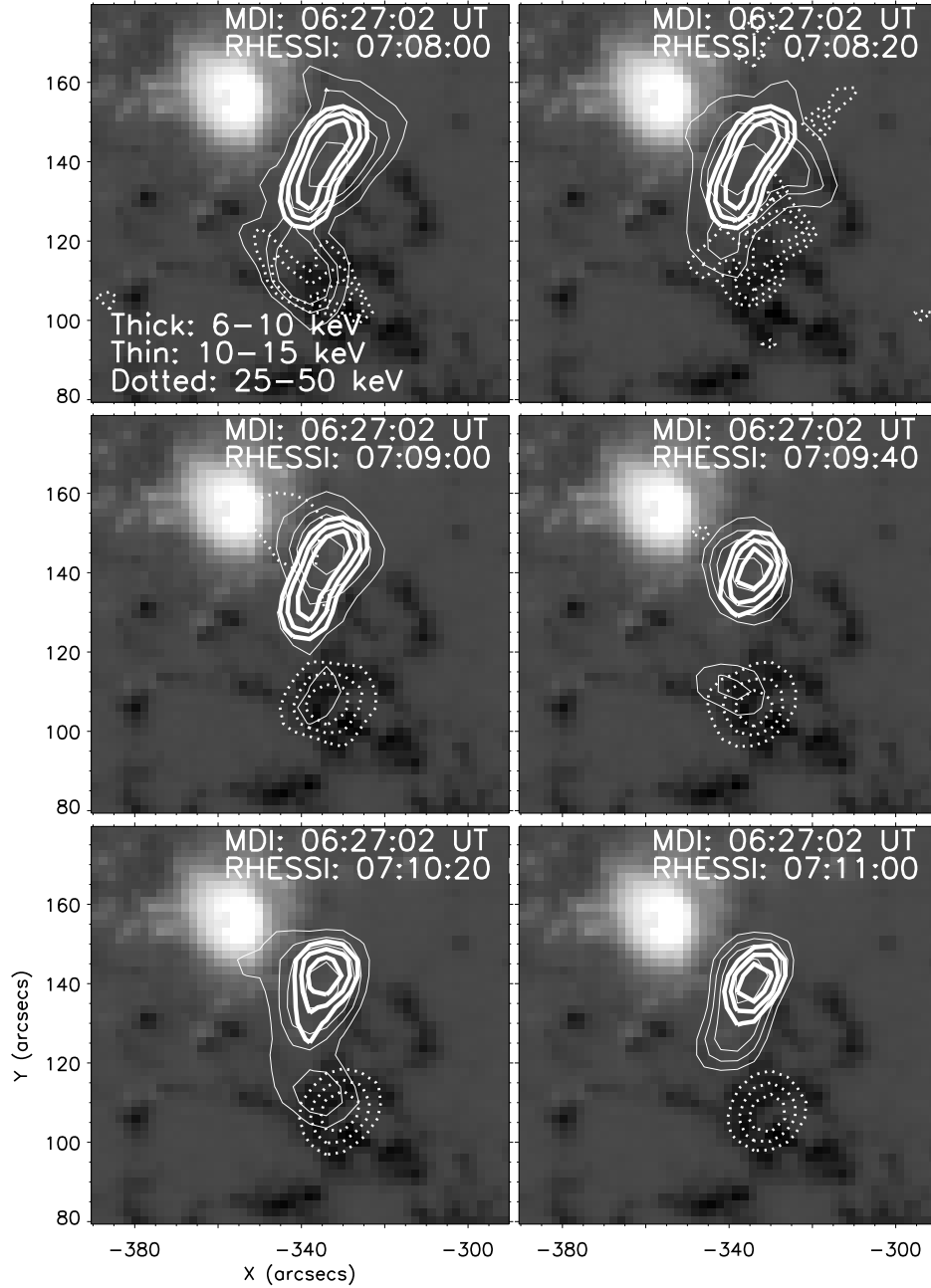


Fig. 6.— As in Fig. 2, MDI magnetic field is plotted with *RHESSI* observations at the six times. Contour levels of the X-rays are at 40%, 60% and 80% for 25-50 keV (*dotted lines*), and at 50%, 60%, 70%, and 90% for 10-15 keV (*thin lines*), and at 70%, 80%, and 90% at 6-10 keV (*thick lines*).

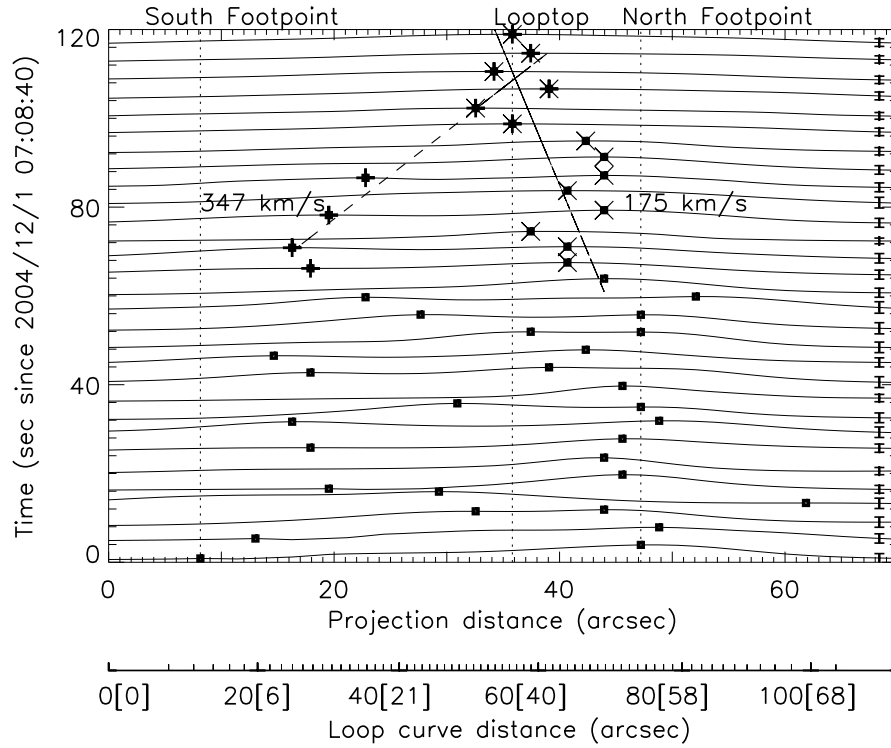


Fig. 7.— As in Fig. 3, evolution of the 10-15 keV brightness profile along the loop in a cadence of 4 s, starting at 07:08:40 UT. The mean velocity is estimated about 175 km s^{-1} for the north footpoint source, and 347 km s^{-1} for the south one (see details in text).